



# Probing supramolecular assembly and charge carrier dynamics toward enhanced photocatalytic hydrogen evolution in 2D graphitic carbon nitride nanosheets

Chengxiao Zhao<sup>a</sup>, Zupeng Chen<sup>b</sup>, Jingsan Xu<sup>c</sup>, Qinqin Liu<sup>d</sup>, Hui Xu<sup>d</sup>, Hua Tang<sup>d,\*\*</sup>, Guisheng Li<sup>e</sup>, Yan Jiang<sup>d</sup>, Feiqiang Qu<sup>d</sup>, Zixia Lin<sup>f</sup>, Xiaofei Yang<sup>a,g,h,\*</sup>

<sup>a</sup> College of Science, Institute of Materials Physics and Chemistry, Nanjing Forestry University, Nanjing, 210037, PR China

<sup>b</sup> Institute for Chemical and Bioengineering, Department of Chemistry and Applied Biosciences, ETH Zürich, 8093, Zürich, Switzerland

<sup>c</sup> School of Chemistry, Physics and Mechanical Engineering, Queensland University of Technology, Brisbane, QLD, 4001, Australia

<sup>d</sup> School of Materials Science and Engineering, Institute for Energy Research, Jiangsu University, Zhenjiang, Jiangsu, 212013, PR China

<sup>e</sup> Key Laboratory of Resource Chemistry of Ministry of Education, Shanghai Key Laboratory of Rare Earth Functional Materials, School of Environmental and Geographical Sciences, Shanghai Normal University, Shanghai, 200234, PR China

<sup>f</sup> Testing Center, Yangzhou University, Yangzhou, 225009, PR China

<sup>g</sup> State Key Laboratory of Photocatalysis on Energy and Environment, Fuzhou University, Fuzhou, 350116, PR China

<sup>h</sup> Key Laboratory for Photonic and Electronic Bandgap Materials, Ministry of Education, School of Physics and Electronic Engineering, Harbin Normal University, Harbin, 150025, PR China

## ARTICLE INFO

### Keywords:

g-C<sub>3</sub>N<sub>4</sub> nanosheets  
Hydrogen evolution  
Ultrafast spectroscopy  
Water splitting  
Supramolecular assembly

## ABSTRACT

Two-dimensional graphitic carbon nitride (2D g-C<sub>3</sub>N<sub>4</sub>) nanostructures have been the focus of substantial research interest recently owing to their promising photoactive properties for use in solar-to-fuel conversion. However, the synthesis of 2D g-C<sub>3</sub>N<sub>4</sub> nanomaterials remains a significant challenge. Here we successfully synthesized 2D g-C<sub>3</sub>N<sub>4</sub> nanosheets via a supramolecular chemistry approach. 2D g-C<sub>3</sub>N<sub>4</sub> nanostructures not only enhance the visible light-harvesting property but also provide more catalytic sites for improved hydrogen evolution reaction (HER). More importantly, we describe experimental findings concerning the dynamics of charge and energy transfer by using ultrafast spectroscopy in combination with in-situ electron spin resonance (ESR) characterization. The mechanistic investigation reveals that the introduction of a benzene-substituted melamine motif can remarkably accelerate the electron-hole separation and suppress the recombination of photogenerated charge carriers. The carrier separation dynamics is expected to be tailored by engineering the surface and morphology of g-C<sub>3</sub>N<sub>4</sub>, which favors enhanced solar photocatalytic HER efficiency.

## 1. Introduction

Natural photosynthesis in green plants has inspired world efforts to explore advanced semiconductor photocatalysts for solar-driven hydrogen production from water. Over the past few decades, metal-containing semiconductors have been intensively investigated because they combine the merits of tunable light harvesting ability, efficient charge transport and superior catalytic performance, thus satisfying the essential criteria for effective visible-light photocatalytic water splitting [1–11]. Although several metal-containing semiconductors have been developed as the hydrogen-evolving catalysts for the photocatalytic water splitting [12–16], they often suffer from problems such as cost

ineffectiveness, high toxicity, or poor photo-/chemical stability. The development of low-cost, highly stable and active visible light-driven photocatalysts with well-defined stoichiometry and morphology remains a substantial challenge.

In 2009, the discovery of polymeric graphitic carbon nitride (g-C<sub>3</sub>N<sub>4</sub>) semiconductor led to a new era of developing metal-free photocatalytic materials in energy conversion and environmental remediation [17], which has been demonstrated to be a “sustainable” photocatalyst possessing the features of non-toxicity, low price, high stability, tunable band structure and visible-light response [18]. The emergence of both electronic and structural variety in g-C<sub>3</sub>N<sub>4</sub> has opened new avenues for the design and controllable synthesis of advanced visible-

\* Corresponding authors at: College of Science, Institute of Materials Physics and Chemistry, Nanjing Forestry University, Nanjing, 210037, PR China.

\*\* Corresponding author.

E-mail addresses: [tanghua@mail.ujes.edu.cn](mailto:tanghua@mail.ujes.edu.cn) (H. Tang), [xiaofei.yang@njfu.edu.cn](mailto:xiaofei.yang@njfu.edu.cn) (X. Yang).

<https://doi.org/10.1016/j.apcatb.2019.117867>

Received 26 January 2019; Received in revised form 15 May 2019; Accepted 14 June 2019

Available online 16 June 2019

0926-3373/ © 2019 Elsevier B.V. All rights reserved.

light-responsive photocatalytic materials and potential catalytic applications [19–21]. Despite its unique physicochemical properties, the photocatalytic efficiency of  $g\text{-C}_3\text{N}_4$  is often limited by its intrinsic drawbacks. For example, the fast recombination of photo-induced electron-hole pairs is detrimental to the efficient utilization of photo-charges due to its relatively low charge carrier mobility. Other demerits including the poor electrical conductivity, insufficient visible light utilization, low specific surface area, densely stacked and irregular microstructure, also impact its photo(electron)catalytic performance [22,23].

To date, extensive efforts have been devoted to improve the hydrogen evolution reaction (HER) efficiency with special emphasis on the morphology regulation [24–26] and molecular engineering of  $g\text{-C}_3\text{N}_4$  [27,28]. Compared with the bulk counterpart, nanostructured  $g\text{-C}_3\text{N}_4$  materials with controllable dimensions demonstrate a more efficient electron-hole separation and enhanced charge transport, resulting in a highly improved photocatalytic activity.  $g\text{-C}_3\text{N}_4$  was conventionally obtained by calcining different precursors such as melamine, dicyandiamide, urea, or thiourea at high temperature, resulting in the formation of irregular and agglomerated structures with low photocatalytic activity. In the past few years, a variety of strategies including elemental doping [29–32], chemical copolymerization [33–35], controllable thermal polymerization [36–38], and templating [39–41] have been exploited to tailor the structure and morphology of  $g\text{-C}_3\text{N}_4$  for enhanced photocatalysis. Among these, the functionalization of  $g\text{-C}_3\text{N}_4$  by chemical copolymerization of precursors is of particular interest because it is an effective approach for tuning the band structure at the molecular level. As an example, the symmetrical and intermolecular Lewis acid-base interaction between the cyanuric acid and melamine leads to formation of the hydrogen-bonded supramolecular preorganization, and the subsequent treatment at high temperature yields well-organized  $g\text{-C}_3\text{N}_4$  nanostructures [42–45].

So far, there has been remarkable progress in fabricating  $g\text{-C}_3\text{N}_4$  nanostructures for highly improved photocatalytic hydrogen evolution from water splitting, however, it still remains a great challenge to produce two-dimensional (2D) large-aspect-ratio  $g\text{-C}_3\text{N}_4$  nanosheets with high performance. Meanwhile, the design and controllable synthesis of ultra-large  $g\text{-C}_3\text{N}_4$  nanosheets via asymmetric polymerization of precursors has been rare. Furthermore, understanding the dynamics interplay and evolution of the photoinduced charge carriers in 2D  $g\text{-C}_3\text{N}_4$  nanostructures is of fundamental scientific interest, and it is also of central importance for promising applications of  $g\text{-C}_3\text{N}_4$  materials in solar-driven photocatalytic water splitting. Herein, we present a preorganization approach based on asymmetric intermolecular assembly of precursors to employ a combination of melamine with benzene-substituted melamine (2,4-diamino-6-phenyl-1,3,5-triazine) as the Lewis base and copolymerize with cyanuric acid. The subsequent calcined  $g\text{-C}_3\text{N}_4$  materials possess ultrathin 2D lamellar nanostructures, enhanced light absorbance in the visible light region, and accelerated electron-hole separation and charge transport, making them promising hydrogen-evolving catalysts for solar-driven photocatalytic water splitting. In this work, we systematically study the effects of employed benzene-substituted melamine on the morphology, chemical and crystal structure of  $g\text{-C}_3\text{N}_4$  materials. On the basis of the insights gained from time-resolved ultrafast spectroscopic studies and in-situ ESR characterizations, we describe the mechanism that accounts for the improved HER performance in large-area 2D  $g\text{-C}_3\text{N}_4$  nanosheets.

## 2. Experimental

### 2.1. Preparation of assembled complexes and $g\text{-C}_3\text{N}_4$

The supramolecular complexes were prepared by mixing cyanuric acid (C), melamine (M), and 2,4-diamino-6-phenyl-1,3,5-triazine (Mp) with molar ratios of 1 : (1- $n$ ) % :  $n$  % (the amount of C was held at 40 mmol, whereas the  $n$  value was 5, 10, 20, 30, respectively) in

ethanol (100 mL), and stirring vigorously for 8 h at room temperature. The obtained white intermediates labelled as CM-P $n$  ( $n$  = 5, 10, 20, 30) were obtained by centrifugation and dried at 60 °C in *vacuum*. After that the dried CM-P $n$  were placed in a muffle furnace for thermal polymerization. The samples were heated to 550 °C with a heating rate of 2.3 °C min<sup>-1</sup>, and then hold for 4 h. After cooling to room temperature, the faint yellow to brown powders CN-P $n$ , ( $n$  = 5, 10, 20, 30) were collected. The synthetic yields for all CN-P $n$  were around 20 wt %. With the same procedure, a carbon nitride reference (CN) was prepared by sintering the hydrogen-bonded supramolecular complex CM, which was obtained by copolymerizing cyanuric acid and melamine with a molar ratio of 1:1 in ethanol.

### 2.2. Characterization

Scanning electron microscopy (SEM), transmission electron microscopy (TEM), and Atomic force microscopy (AFM) observations were performed with a JSM-7001 F, Tecna 12, and MFP-3D Asylum Research, respectively. X-ray powder diffraction patterns were collected by an Ultima IV X-ray diffractometer, using Cu K $\alpha$  radiation with the 2 $\theta$  range from 5° to 50° at a scan rate of 10° min<sup>-1</sup>. Fourier transform infrared (FTIR) spectra were recorded with a Nicolet Model Nexus 470 FT-IR instrument. The samples were pressed with KBr into pellets. N<sub>2</sub> adsorption/desorption performance was taken on the high speed automatic surface and porosity analyzer TriStar II 3020. <sup>13</sup>C cross-polarization magic angle spinning (CP-MAS) solid-state NMR spectra were recorded with an AVANCE III HD 400. Photoluminescence (PL) spectra were measured on a QuantaMaster™ 40 with the excitation wavelength of 395 nm. The UV–vis diffuse reflection spectroscopy (DRS) measurements were recorded by a UV2600 spectrophotometer using BaSO<sub>4</sub> as the reference.

Photocurrent response, Mott-Schottky plots, electrochemical impedance spectroscopy (EIS) measurements of these samples were recorded on an electrochemical workstation (CHI-760E, China). Catalysts (5 mg), ethanol (250  $\mu$ L), ethylene glycol (250  $\mu$ L), and Nafion solution (5 wt %, 40  $\mu$ L) were mixed and dip-coated on the FTO conducting glass to prepare FTO/sample electrode. Na<sub>2</sub>SO<sub>4</sub> aqueous solution (0.1 M, pH = ca. 7) was used as the supporting electrolyte. X-ray photoelectron spectra (XPS) was investigated using a Thermo ESCALAB MKII with Al K $\alpha$  radiation. The electron spin resonance (ESR) spectra were collected using a Bruker model A300 spectrometer under irradiation, in which 2,2,6,6-tetramethyl-1-piperidine-*N*-oxyl (TEMPO) and 5, 5-dimethyl-1-pyrroline N-oxide (DMPO) were used as photogenerated electrons/holes and radicals spin-trapping reagents, respectively. The electron paramagnetic resonance (EPR) spectra were carried out by JESFA200. The femtosecond pump-probe transient absorption spectra (TAS) were performed using a regenerative amplified Ti : sapphire laser system (Coherent: 800 nm, 70 fs, 6 mJ/pulse, and 1 kHz repetition rate) and a femto-TA 100 spectrometer (Time-Tech Spectra). The experiment details followed the description in the literature [46].

Photocatalytic H<sub>2</sub> evolution experiments from water were performed in a gas-closed circulation system (CEL-SPH2N-D9, CEAULight, China) with a Pyrex top-irradiation reaction vessel. The visible-light source was provided by a 300 W Xe-lamp (CEL-HXF300, CEAULight, China) equipped with a 420 nm cutoff filter. In the photocatalytic H<sub>2</sub> production reaction, the as-prepared photocatalyst (10 mg) was dispersed in 50 mL triethanolamine (10 vol%) aqueous solution containing co-catalyst Pt (3 wt%) photo-deposited on the photocatalysts. The circulation system was kept vacuum and the reaction vessel was sustained at 6 °C through cooling water. The amount of H<sub>2</sub> evolved through light irradiation was determined with a gas chromatography (GC-7920).

## 3. Result and discussion

The precursor complexes CM, and CM-P $n$  ( $n$  = 5, 10, 20, 30) were investigated by scanning electron microscopy (SEM). CM showed a

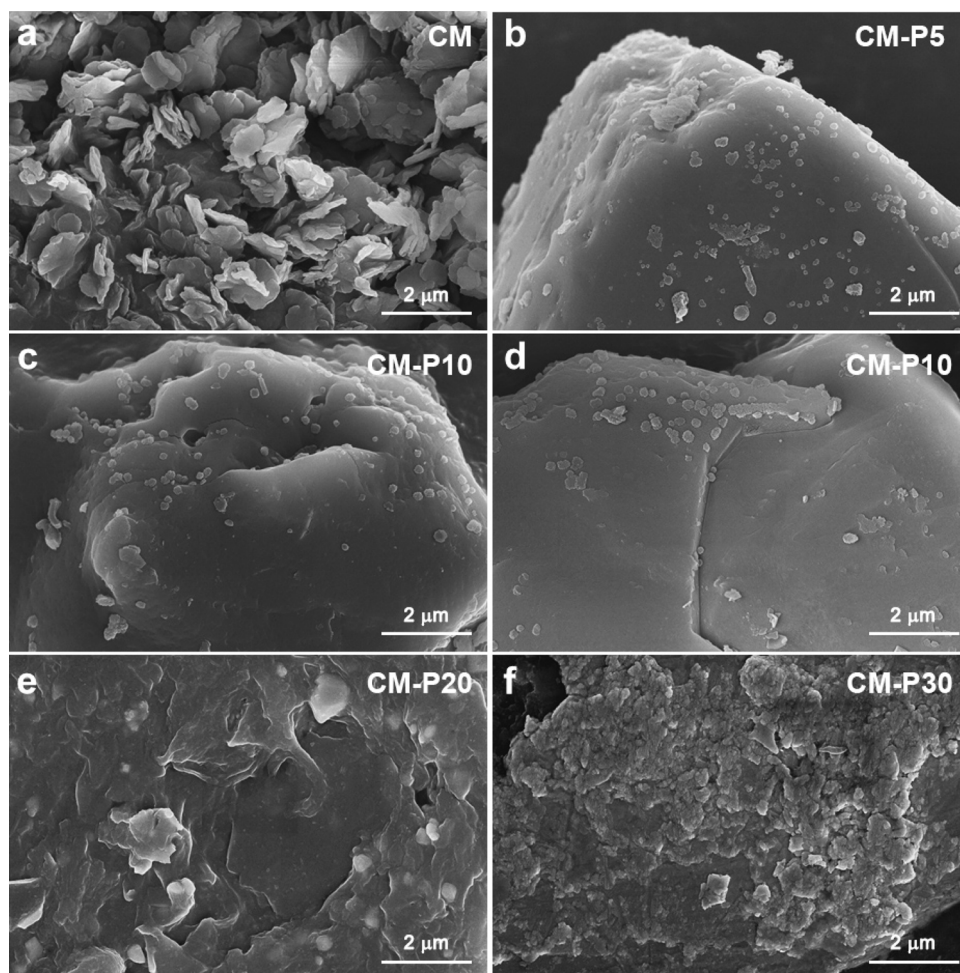


Fig. 1. SEM images of the preorganized complexes (a) CM, (b) CM-P5, (c, d) CM-P10, (e) CM-P20, and (f) CM-P30.

porous disk-like morphology (Fig. 1a), while CM-P5 and CM-P10 exhibited a smooth sedimentary rock-like morphology with small amount of disk-like nanoparticles on the surface (Fig. 1b–d). The wrinkling morphology and rough geomorphology were observed in CM-P20 and CM-P30 (Fig. 1e,f), respectively. These results show that the copolymerization of a small amount of Mp dramatically changes the morphology of the preformed complexes, while further increasing the amount of Mp from 10 to 30 results in rough surface. Fig. 2 shows the SEM images of CN and CN-Pn ( $n = 5, 10, 20, 30$ ). Perforated platelets with a diameter of ca.  $1.3 \mu\text{m}$  were observed in CN, while lamella-like morphologies with stacked nanosheets were found in CN-Pn ( $n = 5, 10, 20, 30$ ). In addition, the smooth and thin lamellas were constructed when Mp content was 10% (Fig. 2c,d), but rough and thick laminar morphologies were obtained when Mp content exceeded 10% (Fig. 2e, f). It is suggested that the presence of a moderate amount of added benzene-substituted Mp is beneficial for the formation of modified large-aspect-ratio g- $\text{C}_3\text{N}_4$  sheets.

The powder X-ray diffractions (XRD) patterns of all calcined products exhibit two peaks centered at  $12.8^\circ$  and  $27.7^\circ$  (Fig. 3a), which correspond to the (100) and (002) plane of heptazine-based g- $\text{C}_3\text{N}_4$ , respectively [47,48]. The Fourier-transform infrared spectroscopy (FTIR) analysis of all samples (Fig. 3b) showed the characteristic stretching vibrations of heptazine units in the region of  $1237\text{--}1640 \text{ cm}^{-1}$ , and the out-of-plane bending of heptazine units at  $810 \text{ cm}^{-1}$  [47,49]. However, no difference could be distinguished between these samples. In addition, solid-state  $^{13}\text{C}$  cross-polarization magic angle spinning (CP-MAS) nuclear magnetic resonance (NMR) spectra of these samples showed the characteristic chemical shifts of

$\text{C}_{3\text{N}}$  and  $\text{C}_{\text{N-NHx}}$  in the heptazine units, which were centered at 159 ppm and 167.2 ppm (Fig. 6a), respectively. These results evidence the formation heptazine-based carbon nitride materials, and the small amount of Mp can hardly influence the construction units and their stacking structures.

The porosity of CN and CN-Pn was examined by nitrogen sorption experiments at 77 K. In Fig. 3c, the nitrogen isotherms of all samples exhibit the typical type IV isotherms with H3-type hysteresis loops at the relative pressure range of 0.7–1.0, which is a characteristic of mesoporous structure [50]. The specific surface areas evaluated based on Brunauer-Emmett-Teller (BET) method are 45, 28, 63, 60, and  $44.7 \text{ m}^2/\text{g}$  for CN, CN-P5, CN-P10, CN-P20, and CN-P30, respectively. This result demonstrates that introducing moderate amount of Mp can increase the specific surface area of carbon nitride. Furthermore, the UV–vis diffuse reflectance spectra (DRS) of these carbon nitrides showed a typical absorption band in the 350–450 nm region (Fig. 3d). With the increase of Mp content in the precursor mixtures, the red-shifted adsorption edge, an absorption shoulder peak arising at 480 nm, and an enhanced absorption in the region of 500–800 nm were observed in the calcined products, which were beneficial for the absorption of visible light.

The photocatalytic HER performance of CN and CN-Pn ( $n = 5, 10, 20, 30$ ) was performed under visible light irradiation in the presence of Pt as a co-catalyst and triethanolamine (TEOA) as a sacrificial agent. As shown in Fig. 4a, the time courses of the hydrogen production performance for all the photocatalysts show that the produced  $\text{H}_2$  amount increased linearly with the irradiation time, and the  $\text{H}_2$  evolution activities were improved after Mp modifying CN. The increased HER performance correlated well with the BET surface areas, indicating that



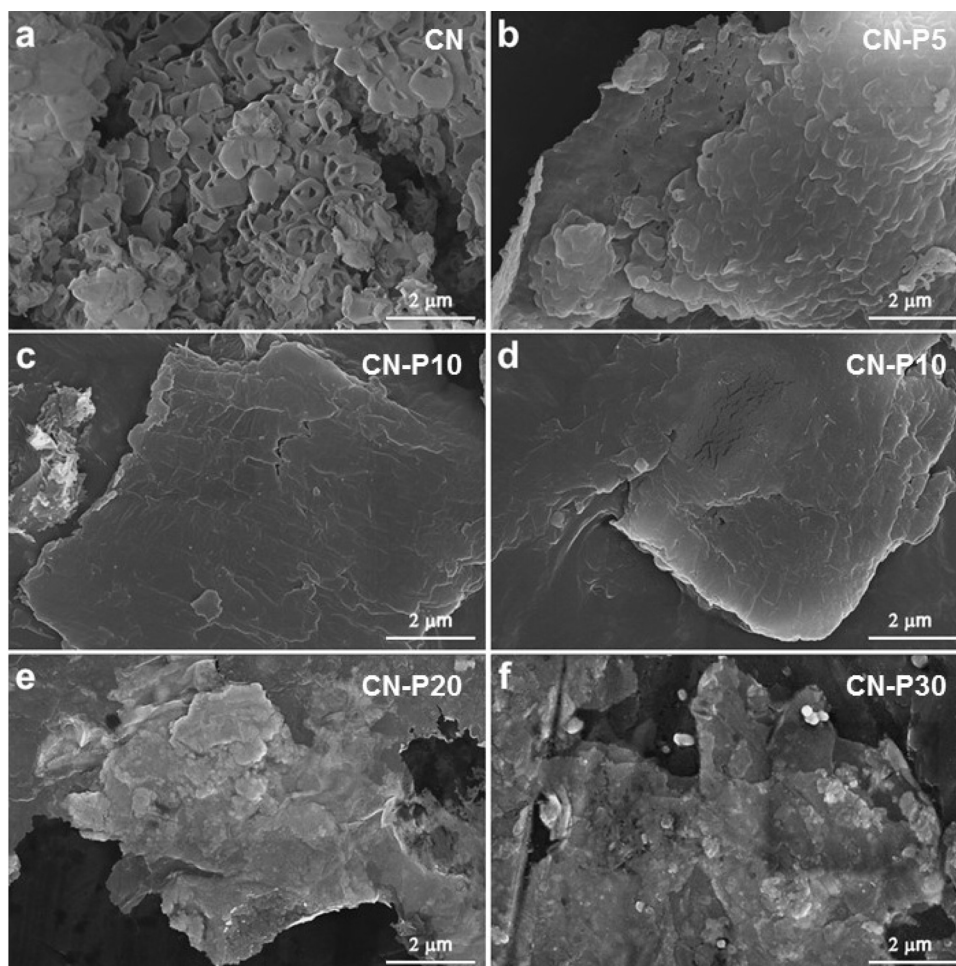


Fig. 2. SEM images of the g-C<sub>3</sub>N<sub>4</sub> samples (a) CN, (b) CN-P5, (c, d) CN-P10, (e) CN-P20, and (f) CN-P30.

the larger BET surface area is beneficial for the photocatalytic activity. As shown in Fig. 4b, CN-P10 showed the highest HER rate of  $2393 \mu\text{mol g}^{-1} \text{h}^{-1}$ , which was about 3-fold to that of CN ( $811 \mu\text{mol g}^{-1} \text{h}^{-1}$ ) and 68-fold to that of the g-C<sub>3</sub>N<sub>4</sub> synthesized from melamine only [51]. Furthermore, it delivers a constant HER rate in five cycling sequences, indicating its high stability for photocatalysis (Fig. 4c, d). The apparent quantum efficiency (AQE) of CN-P10 at 420, 450 and 520 nm monochromatic light were calculated to be 10.6%, 6.4%, and 1.5% (Table S1).

To understand the HER enhancement of CN-P10 as compared to CN, their structures and compositions were further investigated. TEM images of CN exhibit the flaky and ultrathin nanosheets with curly edges (Fig. 5a,c), while CN-P10 shows larger nanosheets with little curly edges (Fig. 5b,d). Furthermore, atomic force microscope (AFM) images show that the sheet-like sample CN-P10 exhibits an average thickness of 4.5 nm (Fig. 5e,f and Fig. S1). Although the addition of Mp increases the BET surface area and the photocatalytic properties of the carbon nitrides, the signal of phenyl is not found in solid-state <sup>13</sup>C CP-MAS NMR spectrum of CN-P10 (Fig. 6a). Moreover, only C and N elements were detected on the surface of CN-P10 by the survey XPS spectra (Fig. 6b). The chemical valence states in CN and CN-P10 were further investigated by high resolution C 1s and N 1s XPS analysis. The C 1s spectrum of CN-P10 shows a strong peak at 288.2 eV (Fig. 6c), which can be attributed to the sp<sup>2</sup>-bonded carbon atoms (N=C-N) involved in heptazine units. In addition, a weak peak at 284.7 eV can be ascribed to amorphous carbon, contaminated carbon or surface carbon. For the N 1s spectrum of CN-P10 (Fig. 6d), the strong broad peak can be fitted by three peaks at 398.8, 400.3, and 401.5 eV, which are assigned

to the sp<sup>2</sup>-hybridized nitrogen in heptazine unit (C-N = C), the tertiary nitrogen N-(C)<sub>3</sub>, and amino carrying N species (C-NH<sub>x</sub>), respectively. Additionally, the weak peak centered at 404.2 eV arise from the positive charge localization in the heptazine. A similar XPS spectrum of CN implies that CN has the same elemental composition and chemical valence state with CN-P10, and that the phenyls in CN-P10 may be carbonization or break away in the process of sintering.

It is well known that the process of photocatalytic H<sub>2</sub> evolution from water involves the generation of photocharges, and the subsequent migration and separation, and recombination within the photocatalysts. Herein, the transient generation of photocurrent and electrochemical impedance spectra (EIS) were used to investigate the photoinduced charge migration and separation properties of CN and CN-P10. As depicted in Fig. 7a, both samples exhibited a sensitive photocurrent response during on/off visible-light irradiation cycles, however, the current density of CN-P10 was nearly 1.3 times higher than that of CN, which strongly suggests the higher mobility of the photoexcited charge carriers and more efficient separation of electron-hole pairs in CN-P10. The EIS Nyquist plots of CN-P10 shows a significantly smaller EIS radius compared to CN (Fig. 7b), indicating a lower charge transfer resistance, resulting in more efficient separation of charge carriers. Moreover, the photoluminescence (PL) spectra show that the emission peak of CN located at 462 nm, while that of CN-P10 red shifts to 510 nm. Meanwhile, the PL intensity of CN-P10 was much weaker than that of CN (Fig. 7c), suggesting the suppressed radiative recombination in CN-P10. This is consistent with the indications of transient photocurrents and EIS Nyquist plots. In order to explore the source of photogenerated electrons for CN and CN-P10, the room-temperature electron

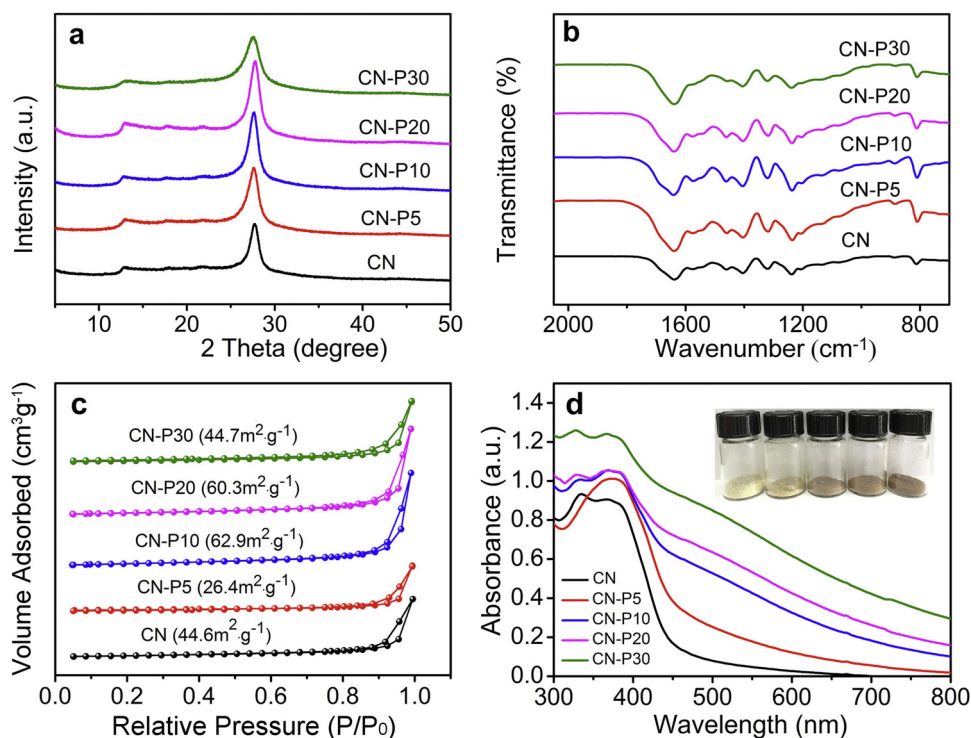


**Fig. 3.** (a) XRD patterns, (b) FT-IR spectra, (c) nitrogen adsorption-desorption isotherms, and (d) UV-vis diffuse reflectance spectra of CN and CN-P $n$  ( $n = 5, 10, 20, 30$ ). Insets in (d) show the photographic images of different samples.

paramagnetic resonance (EPR) spectra were recorded (Fig. 7d). Both CN and CN-P10 exhibited only one single Lorentzian paramagnetic absorption signal with the  $g$  value of 2.0001, originating from the unpaired electrons on  $\pi$ -conjugated CN aromatic heterocyclic rings. However, CN-P10 showed an enhanced EPR signal as compared to CN, suggesting more efficient generation of photoelectrons arising from the redistribution of  $\pi$ -electrons within CN-P10 or the extended delocalization of  $\pi$ -conjugated system [52].

Furthermore, electron spin resonance (ESR) experiments were performed to directly detect the photogenerated electrons and holes under the photocatalytic surrounding. 2,2,6,6-tetramethyl-1-piperidine- $N$ -oxyl (TEMPO), typical spin label molecule, was used for trapping the photogenerated electrons ( $e^-$ ) and holes ( $h^+$ ) on the surface of CN and CN-P10 (Fig. 8a, b). In the dark, the characteristic triplet TEMPO signals with intensity of 1:1:1 were observed in the ESR spectra collected in aqueous solution and acetonitrile solution, while the signal intensity

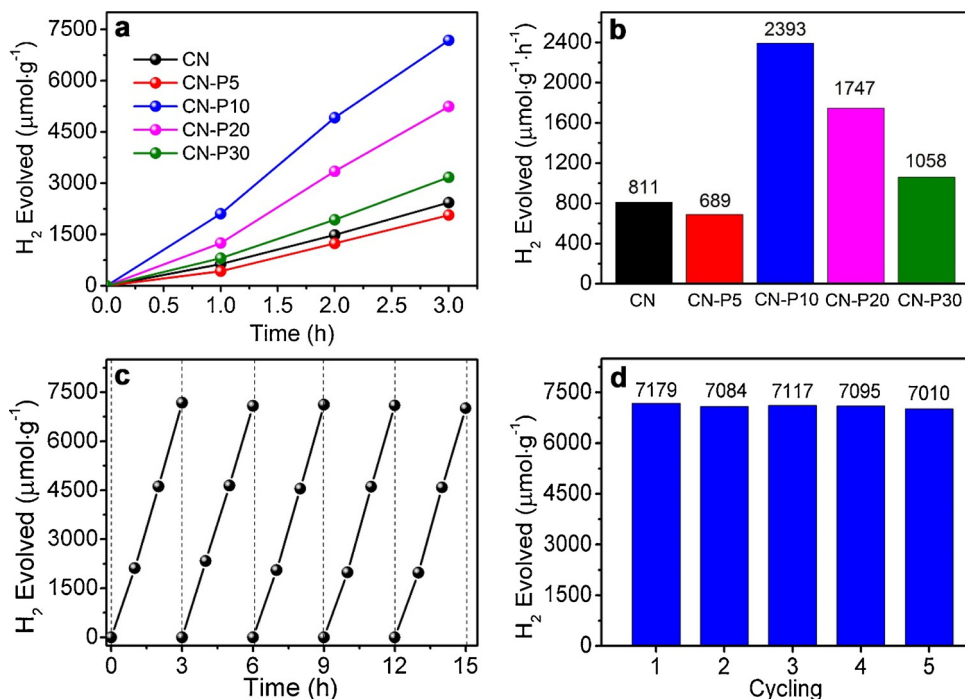


**Fig. 4.** (a) Photocatalytic H<sub>2</sub> evolution performance and (b) average H<sub>2</sub> evolution rates for CN and CN-P $n$ ; (c, d) cycling measurements of H<sub>2</sub> evolution of CN-P10.

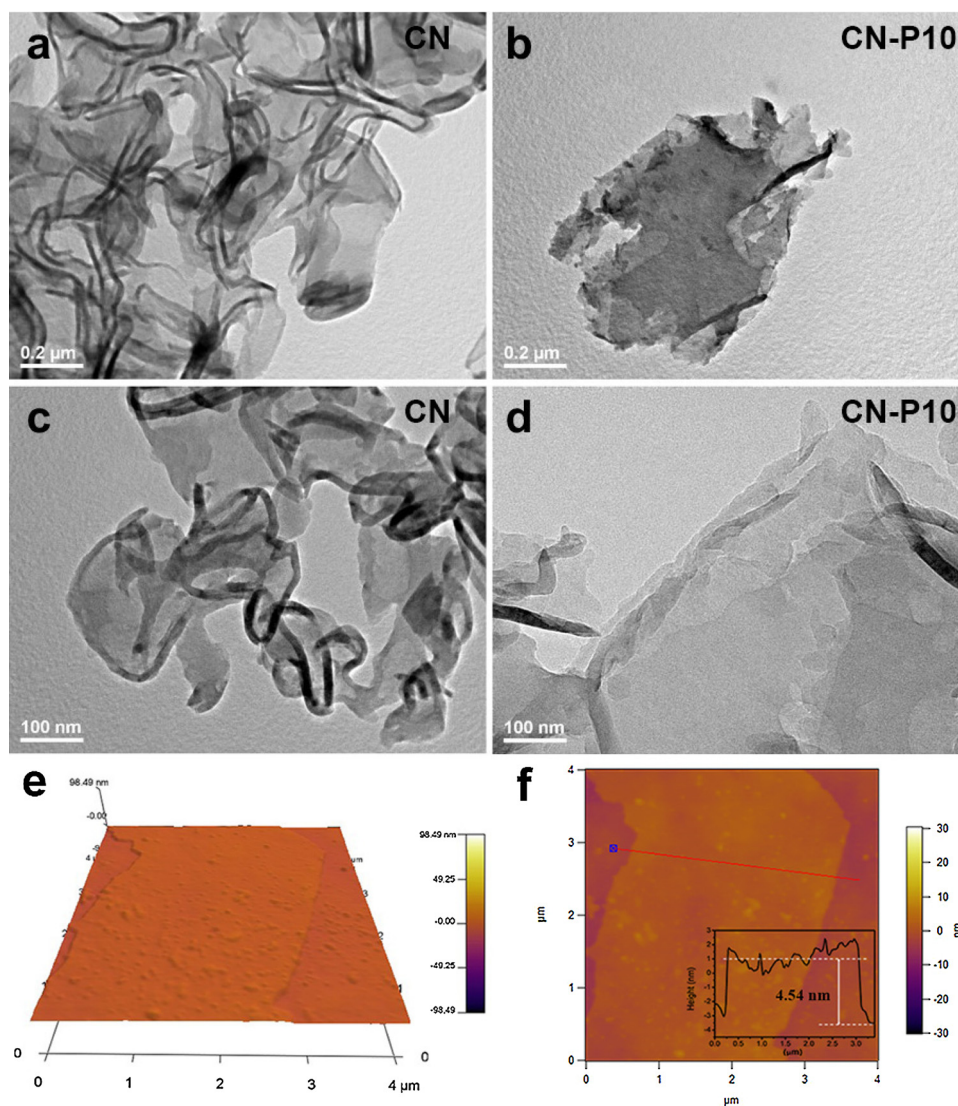


**Fig. 5.** TEM images of (a, c) CN and (b, d) CN-P10; (e, f) AFM images of the sheet-like sample CN-P10 and the corresponding height profile.

dramatically decreased under visible light irradiation for 10 min. This can be explained by the fact that TEMPO molecules underwent a reduction to corresponding hydroxylamine (TEMPOH) in aqueous system by trapping electrons and underwent an oxidation to corresponding oxoammonium cations ( $\text{TEMPO}^+$ ) in acetonitrile by combining with holes (Fig. 8e) [53]. This phenomenon can explicitly verify the production of electrons and holes from photoexcited CN and CN-P10. A careful examination reveals that the attenuation of TEMPO signals in the aqueous dispersion and acetonitrile dispersion of CN-P10 is much more obvious, indicating an enhancement of generation and reactivity of photoinduced electrons and holes.

The active radical species involved in photocatalytic  $\text{H}_2$  evolution were further investigated by the 5,5-dimethyl-1-pyrroline-*N*-oxide (DMPO) spin-trapped ESR spectroscopy. DMPO that acts as a typical radical scavenger can trap the superoxide radicals ( $\text{O}_2^{\cdot-}$ ) to form the  $\text{DMPO}\cdot\text{O}_2^-$  adducts, and capture the hydroxyl radicals ( $\text{OH}\cdot$ ) to transform into the  $\text{DMPO}\cdot\text{OH}$  adducts (Fig. 8e). In Fig. 8c and d, neither CN nor CN-P10 showed any signal in dark, but the signals of  $\text{DMPO}\cdot\text{O}_2^-$  and  $\text{DMPO}\cdot\text{OH}$  adducts could be monitored after visible light irradiation for 10 min. A set of distinct four broad peaks observed in the ESR spectra from methanol dispersion (Fig. 8c) was attributed to the  $\text{DMPO}\cdot\text{O}_2^-$  adducts, and the typical 1:2:2:1 quartet signal detected in aqueous dispersion (Fig. 8d) were consistent with the characteristics of

$\text{DMPO}\cdot\text{OH}$  adducts. These results reflect that both the superoxide radicals ( $\text{O}_2^{\cdot-}$ ) and hydroxyl radicals ( $\text{OH}\cdot$ ) can generate on the surface of CN and CN-P10 only under light irradiation. In addition, the stronger  $\text{DMPO}\cdot\text{O}_2^-$  and  $\text{DMPO}\cdot\text{OH}$  signals of CN-P10 suggest the more photoinduced electrons formed in CN-P10 again.

To further understand the charge carrier dynamics, the transient-absorption (pump-probe) spectroscopic (TAS) measurements of CN and CN-P10 were carried out. In Fig. 9a, only a broad band negative absorption with a maximum at 565 nm appeared in the region 430–760 nm for CN within a few picoseconds, indicating the ground-state bleach features and stimulated emission [54]. In addition, the TAS spectra of CN-P10 showed a positive absorption in 650–780 nm region (Fig. 9b) arising from absorption of excited-state electrons (Fig. 9e). Moreover, the positive absorption signal decreased and inverted to a negative value at delay time of  $\sim 1$  ns, which may be caused by the charge separation states formed with the photogenerated electrons or holes in different traps in CN-P10 [55,56]. The obvious difference of TAS for CN and CN-P10 suggests the more efficient electron-hole separation in the CN-P10.

The kinetics profiles of CN and CN-P10 were measured at the probing wavelength of 500 nm and 565 nm (Fig. 9c,d), respectively. In both cases, the immediate decrease traces (delay time  $< 1$  ps) reflect the initial generation and cooling of hot excitons (Fig. 9 insets) [57,58].



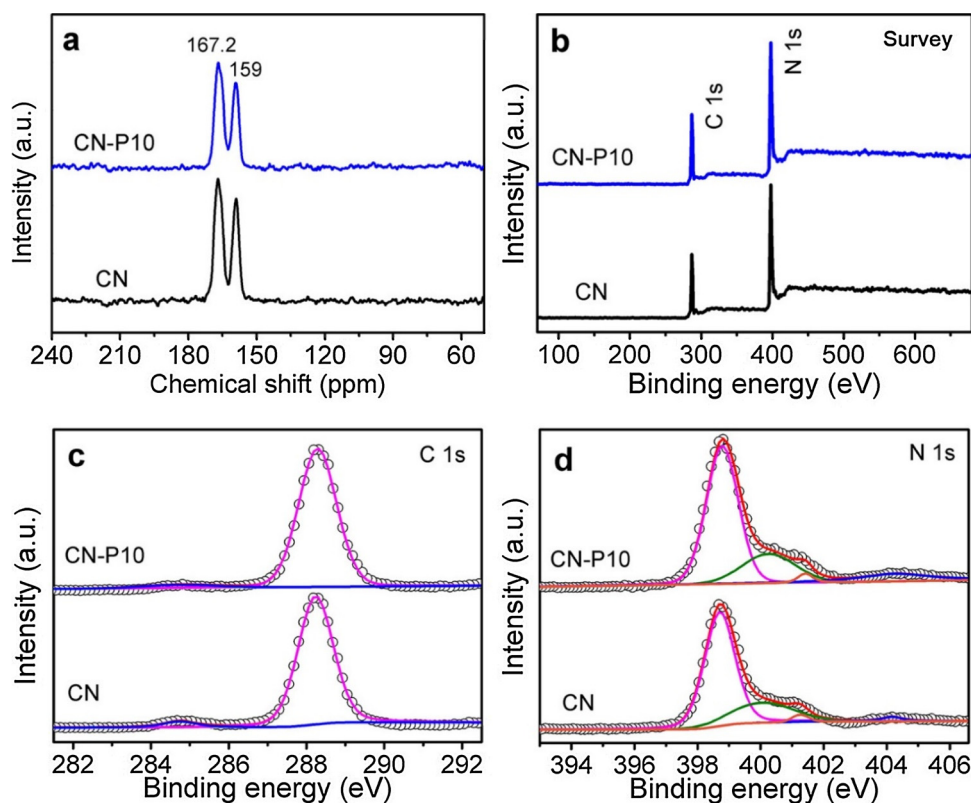


Fig. 6. (a) Solid-state  $^{13}\text{C}$  CP-MAS NMR spectra, (b) survey XPS spectra, (c) C 1s XPS spectra, and (d) N 1s XPS spectra of CN and CN-P10.

The following recovery traces of CN ( $2^{\sim}400$  ps) and CN-P10 ( $2^{\sim}150$  ps) fitted by a bi-exponential decay function account for the electron trapping from the band edge to certain band-gap trap states (Fig. 9e). The late-time monotone decreasing kinetic traces superimposing on the bleach recovery traces implies the reverse hole transfer (RHT) processes from adsorbates to the substrates. For the bleach recovery trace of CN

(delay time  $< 400$  ps), the rising  $\Delta A$  signal converged to a non-zero extremum of  $\sim -2.1$  mOD (Fig. 9c) with two-time constants of  $\tau_1 = 3.2$  ps and  $\tau_2 = 46.5$  ps. Moreover, the fluorescence emission of CN was at ca. 462 nm (i.e. 2.68 eV, below its bandgap energy of 2.72 eV), suggesting that the radiative electron-hole recombination could originate from two trap states which are located in close

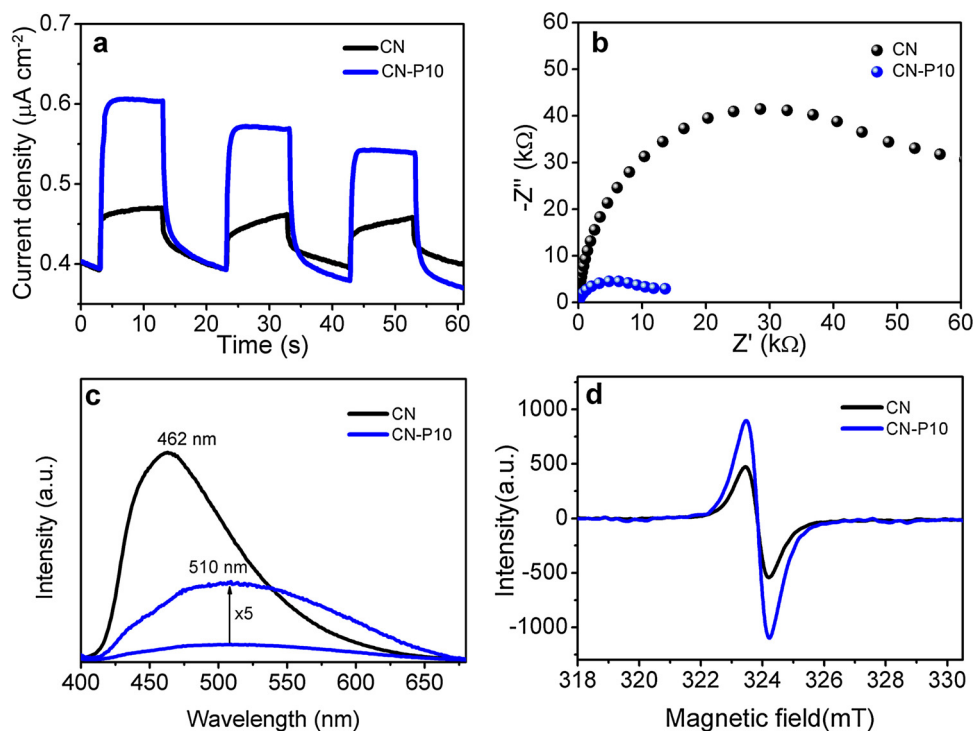
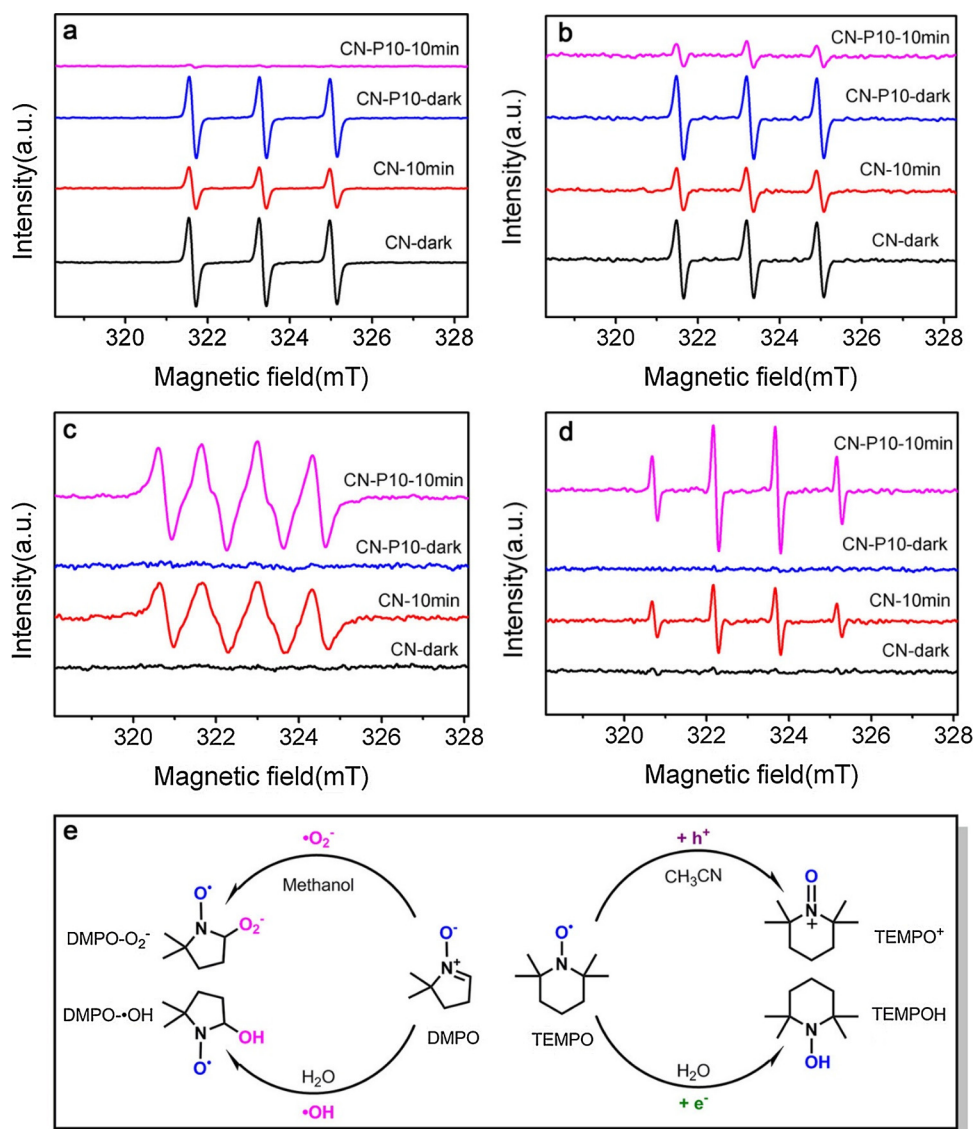


Fig. 7. (a) Photocurrent responses curves, (b) EIS Nyquist plots, (c) Photoluminescence spectra, and (d) EPR spectra of CN and CN-P10.



**Fig. 8.** ESR signal of TEMPO radicals reacting with (a) photoinduced electrons in aqueous dispersion of CN and CN-P10 and (b) holes in acetonitrile dispersion of CN and CN-P10; ESR signals of (c) DMPO- $\cdot\text{O}_2^-$  adducts in methanol dispersion over CN and CN-P10 and (d) DMPO- $\cdot\text{OH}$  adducts in aqueous dispersion over CN and CN-P10; (e) Spin-trapping mechanism of TEMPO and DMPO.

proximity of the CB edge (Fig. 9e) [59,60]. As the delay time exceeding 400 ps, an observed growth kinetic process converged to a negative plateau (with a magnitude of about 3 mOD) paralleling to  $\Delta A = 0$  with a large time constant of 897.1 ps, which reflect photoinduced absorption of the holes transferred reversely from the adsorbates to the VB edge of photocatalyst (Fig. 9e) [57]. Thus, the trapped electrons eventually recombining with the holes transferred back from the adsorbates resulted in an obvious long tail followed the RHT growth (Fig. 9c).

Likewise, the CN-P10 exhibited a similar kinetic trace consisted of charge separation, ground-state bleach recovery, and RHT trace (Fig. 9d). However, the ground-state bleach recovery trace shortened to the delay time of 150 ps with two-time constants of  $\tau_1 = 2.2$  ps and  $\tau_2 = 26.9$  ps and  $\Delta A$  signal converged to the extremum of -2.5 mOD, indicating shallower trap and more trapped excitons, which corresponds to its fluorescence emission centered at 510 nm (i.e. 2.43 eV lowered its bandgap energy of 2.45 eV slightly, Fig. 7c). The RHT trace of CN-P10 featured a time constant of 517.7 ps, which was shorter than that of CN (897.1 ps), suggesting a much faster interfacial hole transfer from adsorbates to substrates. Unfortunately, the process of the TA signals of CN and CN-P10 eventually recovering to null cannot be

recorded due to the optical delay scanning limit of the pump-probe spectrometer. But a fraction of excited-state electrons in CN-P10 were excited to a higher energy level to form a long-lived charge-separation state (Fig. 9b), which results in increased probability of charge carriers participating in redox reactions.

Besides the above photogenerated electron motion, the CB edges and band gaps of materials matching the potentials of water splitting were investigated. The energy band structures of CN and CN-P10 were determined by Tauc plots, XPS valence band spectra, and Mott-Schottky measurements. The band gaps from Tauc plots were 2.71 eV for CN and 2.45 eV for CN-P10 (Fig. 10a), indicating that CN-P10 displayed a remarkably enhanced visible-light-harvesting ability. Moreover, the narrowed band gap (0.26 eV) and red-shifted and weakened PL peak (Fig. 7c) of CN-P10 suggest that there were more electrons transfer to an excited state of CN-P10 under visible-light irradiation. The conduction bands (CB) were determined with the Mott-Schottky plots. As shown in Fig. 10c, the positive slope of the obtained  $C^{-2}$  values indicates that both samples are n-type semiconductors. The flat band positions of CN and CN-P10 are separately determined to be -1.15 V and -1.21 V vs Ag/AgCl, which confirms their CB bottom of -0.84 V and -0.90 V (normal hydrogen electrode) according to the subsequent



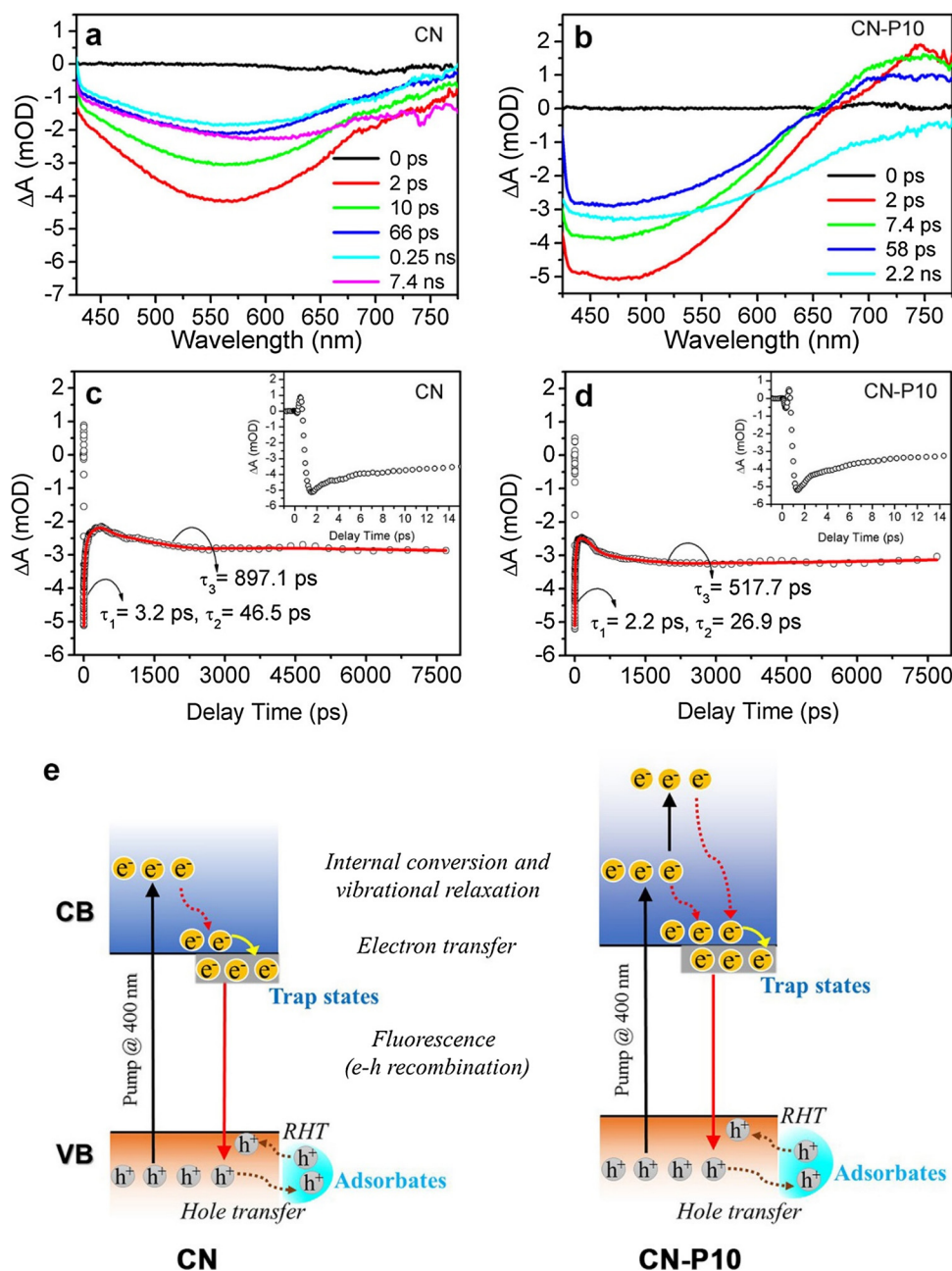


**Fig. 9.** (a, b) Transient absorption spectra of CN and CN-P10 with 400 nm pump excitation at selected delay times; (c, d) transient absorption-time profiles (kinetic traces) of CN and CN-P10 dispersions monitored at 565 and 500 nm; (e) proposed kinetic schemes for the CN and CN-P10 after excitation.

Eqs. (1) and (2) [61].

$$E_{fb} \text{ (vs NHE, pH = 0)} = E_{fb} \text{ (vs Ag/AgCl)} + 0.059 \times \text{pH} + E_{(AgCl)} \quad (1)$$

$$E_{CBM} \text{ (vs NHE)} = E_{fb} \text{ (vs NHE, pH = 0)} - 0.3 \quad (2)$$

Where  $E_{fb}$  (vs Ag/AgCl) is determined on the Mott-Schottky plot,  $E_{(AgCl)}$  is 0.197 V, and the pH is about 7.0. The actual  $E_{CBM}$  (vs NHE) is obtained with the Eq. (2), as the calculated  $E_{fb}$  (vs NHE) is about 0.3 V below the CB minimum (CBM) for undoped n-type semiconductors. Correspondingly, their valence bands (VB) are calculated to be 1.88 V and 1.55 V, which are consistent with the XPS valence band spectra (Fig. 10b). The band structures of CN and CN-P10 are schematically shown in Fig. 10e. The upshifted CB of CN-P10 leads to a larger thermodynamic driving force in photocatalytic hydrogen production.

Combining the results of ESR and band structures of CN and CN-P10, some inferences are proposed. As shown in Fig. 10e, the formation

of  $\cdot O_2^-$  radicals may be induced via direct reduction of dissolved  $O_2$  by photogenerated electrons, since the CB edge potentials of CN (-0.84 V) and CN-P10 (-0.90 V) are more negative than the standard redox potential of  $O_2/\cdot O_2^-$  (-0.046 V vs NHE) [62]. The  $\cdot OH$  radicals might be produced through further conversion of  $\cdot O_2^-$  radicals, because the standard redox potentials of  $OH^-/\cdot OH$  (1.99 V vs NHE) and  $H_2O/\cdot OH$  (2.27 V) are more positive than the VB edge potentials of CN (1.88 V) and CN-P10 (1.55 V). Additionally, the stronger DMPO- $\cdot O_2^-$  radical signals of CN-P10 reflects that more excited electrons occupied the CB edge of CN-P10 due to its narrower band gap energy (2.45 eV), resulting in more potential participation of photocatalytic water splitting. The faster signal attenuation of TEMPO in CN-P10 reflects that the holes in CN-P10 transfer to the adsorbates more rapidly than in CN.

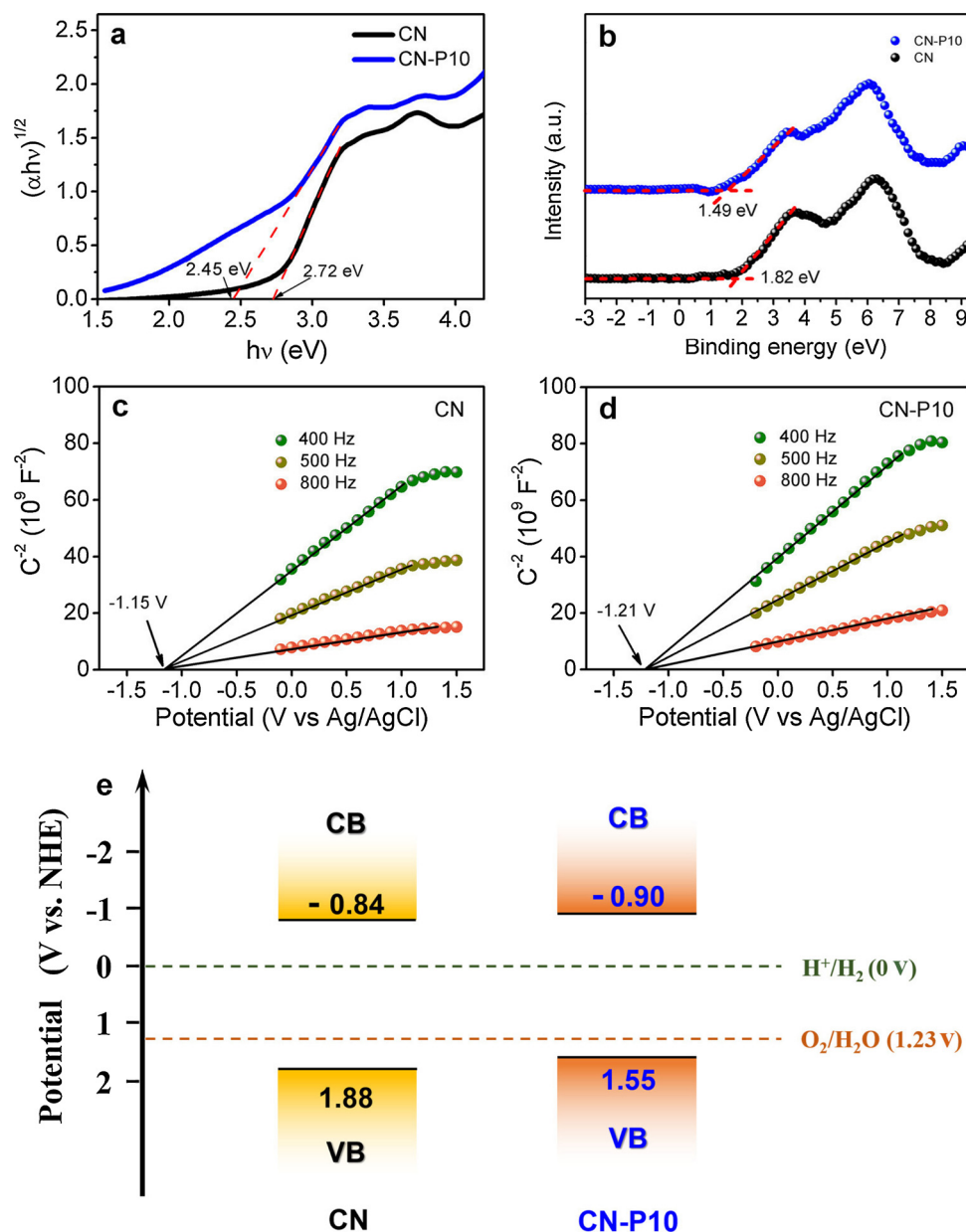


**Fig. 10.** (a) Tauc plots of  $(\alpha h\nu)^{1/2}$  versus  $h\nu$  for the band gap energy, and (b) XPS valence band spectra of CN and CN-P10; (c, d) Mott-Schottky plots (scatters) of CN and CN-P10 collected at different frequencies; (e) CB and VB positions of CN and CN-P10.

#### 4. Conclusions

In summary, we have demonstrated that two-dimensional large-aspect-ratio g-C<sub>3</sub>N<sub>4</sub> nanosheets can be facilely fabricated via thermal copolymerization of the preorganized supramolecular complexes of melamine, cyanuric acid, and 2,4-diamino-6-phenyl-1,3,5-triazine. A small amount of benzene-substituted melamine empowers the g-C<sub>3</sub>N<sub>4</sub> material to undergo a dramatic morphological transformation forming large-aspect-ratio nanostructures. The specific 2D nanostructure not only remarkably enhances the solar exploitation but also obviously improves the resulting photocatalytic HER performance. It is notable that the presented strategy makes it possible to synthesize well-organized 2D g-C<sub>3</sub>N<sub>4</sub> nanosheets instead of the time and energy consuming and low yielded liquid exfoliation approach. More importantly, our research clearly reveals the charge-carrier dynamics based on ultrafast spectroscopic characterization and in-situ ESR measurements. In view of the importance of 2D nanostructures and charge carrier mobility in the photocatalytic water splitting, insightful understanding of charge-

carrier dynamics in the illuminated 2D g-C<sub>3</sub>N<sub>4</sub>-based photocatalysts may help to realize high-performance solar-to-fuel conversion.

#### Declarations of interest

None.

#### Acknowledgements

This work was supported by Six Talent Peaks Project in Jiangsu Province (2015-XCL-026), Natural Science Foundation of Jiangsu Province (BK20171299), Start-Up Fund from Nanjing Forestry University, State Key Laboratory of Photocatalysis on Energy and Environment (SKLPEE-KF201705), Fuzhou University, the National Natural Science Foundation of China (51672113), and QingLan Project of Jiangsu Province. The authors extend their appreciation to the Advanced Analysis and Testing Center, Nanjing Forestry University for the help of materials characterizations.

## Appendix A. Supplementary data

Supplementary material related to this article can be found, in the online version, at doi:<https://doi.org/10.1016/j.apcatb.2019.117867>.

## References

- J.Y. Guo, J. Liang, X.Z. Yuan, L.B. Jiang, G.M. Zeng, H.B. Yu, J. Zhang, Efficient visible-light driven photocatalyst, silver (meta) vanadate: synthesis, morphology and modification, *Chem. Eng. J.* 352 (2018) 782–802.
- Y.O. Wang, H. Suzuki, J.J. Xie, O. Tomita, D.J. Martin, M. Higashi, D. Kong, R. Abe, J.W. Tang, Mimicking natural photosynthesis: solar to renewable H<sub>2</sub> fuel synthesis by Z-scheme water splitting systems, *Chem. Rev.* 118 (2018) 5201–5241.
- J. Qi, W. Zhang, R. Cao, Solar-to-Hydrogen energy conversion based on water splitting, *Adv. Energy Mater.* 8 (2018) 1701620.
- Q.L. Xu, L.Y. Zhang, J.G. Yu, S. Wageh, A.A. Al-Ghamdi, M. Jaroniec, Direct Z-scheme photocatalysts: principles, synthesis, and applications, *Mater. Today* 21 (2018) 1042–1063.
- Y. Guo, P.F. Wang, J. Qian, Y.H. Ao, C. Wang, J. Hou, Phosphate group grafted twinned BiPO<sub>4</sub> with significantly enhanced photocatalytic activity: synergistic effect of improved charge separation efficiency and redox ability, *Appl. Catal. B-Environ.* 234 (2018) 90–99.
- S.J.A. Moniz, S.A. Shevlin, D.J. Martin, Z.X. Guo, J.W. Tang, Visible-light driven heterojunction photocatalysts for water splitting - a critical review, *Energy Environ. Sci.* 8 (2015) 731–759.
- J.R. Ran, J. Zhang, J.G. Yu, M. Jaroniec, S.Z. Qiao, Earth-abundant cocatalysts for semiconductor-based photocatalytic water splitting, *Chem. Soc. Rev.* 43 (2014) 7787–7812.
- Z.G. Yi, J.H. Ye, N. Kikugawa, T. Kako, S.X. Ouyang, H. Stuart-Williams, H. Yang, J.Y. Cao, W.J. Luo, Z.S. Li, Y. Liu, R.L. Withers, An orthophosphate semiconductor with photooxidation properties under visible-light irradiation, *Nat. Mater.* 9 (2010) 559–564.
- X. Feng, P. Wang, J. Hou, J. Qian, C. Wang, Y.H. Ao, Oxygen vacancies and phosphorus codoped black titania coated carbon nanotube composite photocatalyst with efficient photocatalytic performance for the degradation of acetaminophen under visible light irradiation, *Chem. Eng. J.* 352 (2018) 947–956.
- J.-D. Xiao, H.-L. Jiang, Metal-organic frameworks for photocatalysis and photo-thermal catalysis, *Acc. Chem. Res.* 52 (2019) 356–366.
- A. Naldoni, M. Altomare, G. Zoppellaro, N. Liu, S. Kment, R. Zboril, P. Schmuki, Photocatalysis with reduced TiO<sub>2</sub>: from black TiO<sub>2</sub> to cocatalyst-free hydrogen production, *ACS Catal.* 9 (2019) 345–364.
- S. Ma, Y.P. Deng, J. Xie, K.L. He, W. Liu, X.B. Chen, X. Li, Noble-metal-free Ni<sub>3</sub>C cocatalysts decorated CdS nanosheets for high efficiency visible-light-driven photocatalytic H<sub>2</sub> evolution, *Appl. Catal. B-Environ.* 227 (2018) 218–228.
- Q.Y. Li, F.J. Zhao, C. Qu, Q.Y. Shang, Z.H. Xu, L. Yu, J.R. McBride, T.Q. Lian, Two-dimensional morphology enhances light-driven H<sub>2</sub> generation efficiency in CdS Nanoplatelet-Pt heterostructures, *J. Am. Chem. Soc.* 140 (2018) 11726–11734.
- C.M. Wolff, P.D. Frischmann, M. Schulze, B.J. Bohn, R. Wein, P. Livadas, M.T. Carlson, F. Jackel, J. Feldmann, F. Wurthner, J.K. Stolarczyk, All-in-one visible-light-driven water splitting by combining nanoparticulate and molecular co-catalysts on CdS nanorods, *Nat. Energy* 3 (2018) 862–869.
- B. Mahler, V. Hoepfner, K. Liao, G.A. Ozin, Colloidal synthesis of 1T-WS<sub>2</sub> and 2H-WS<sub>2</sub> nanosheets: applications for photocatalytic hydrogen evolution, *J. Am. Chem. Soc.* 136 (2014) 14121–14127.
- R. Chen, P.F. Wang, J. Chen, C. Wang, Y.H. Ao, Synergetic effect of MoS<sub>2</sub> and MXene on the enhanced H<sub>2</sub> evolution performance of CdS under visible light irradiation, *Appl. Surf. Sci.* 473 (2019) 11–19.
- X.C. Wang, K. Maeda, A. Thomas, K. Takanabe, G. Xin, J.M. Carlsson, K. Domen, M. Antonietti, A metal-free polymeric photocatalyst for hydrogen production from water under visible light, *Nat. Mater.* 8 (2009) 76–80.
- K.S. Lakhi, D.H. Park, K. Al-Bahily, W. Cha, B. Viswanathan, J.H. Choy, A. Vinu, Mesoporous carbon nitrides: synthesis, functionalization, and applications, *Chem. Soc. Rev.* 46 (2017) 72–101.
- X. Yang, L. Tian, X. Zhao, H. Tang, Q. Liu, G. Li, Interfacial optimization of g-C<sub>3</sub>N<sub>4</sub>-based Z-scheme heterojunction toward synergistic enhancement of solar-driven photocatalytic oxygen evolution, *Appl. Catal. B-Environ.* 244 (2019) 240–249.
- J.W. Sun, J.S. Xu, A. Grafmueller, X. Huang, C. Liedel, G. Algara-Siller, M. Willinger, C. Yang, Y.S. Fu, X. Wang, M. Shalom, Self-assembled carbon nitride for photocatalytic hydrogen evolution and degradation of p-nitrophenol, *Appl. Catal. B-Environ.* 205 (2017) 1–10.
- S.W. Cao, J.X. Low, J.G. Yu, M. Jaroniec, Polymeric photocatalysts based on graphitic carbon nitride, *Adv. Mater.* 27 (2015) 2150–2176.
- W.H. Niu, Y. Yang, Graphitic carbon nitride for electrochemical energy conversion and storage, *ACS Energy Lett.* 3 (2018) 2796–2815.
- J.W. Fu, J.G. Yu, C.J. Jiang, B. Cheng, G-C<sub>3</sub>N<sub>4</sub>-Based heterostructured photocatalysts, *Adv. Energy Mater.* 8 (2018) 1701503.
- C.C. Dong, Z.Y. Ma, R.T. Qie, X.H. Guo, C.H. Li, R.J. Wang, Y.L. Shi, B. Dai, X. Jia, Morphology and defects regulation of carbon nitride by hydrochloric acid to boost visible light absorption and photocatalytic activity, *Appl. Catal. B-Environ.* 217 (2017) 629–636.
- X.J. She, L. Liu, H.Y. Ji, Z. Mo, Y.P. Li, L.Y. Huang, D.L. Du, H. Xu, H.M. Li, Template-free synthesis of 2D porous ultrathin nonmetal-doped g-C<sub>3</sub>N<sub>4</sub> nanosheets with highly efficient photocatalytic H<sub>2</sub> evolution from water under visible light, *Appl. Catal. B-Environ.* 187 (2016) 144–153.
- Z. Mo, H. Xu, Z.G. Chen, X.J. She, Y.H. Song, J.J. Wu, P.C. Yan, L. Xu, Y.C. Leia, S.Q. Yuan, H.M. Li, Self-assembled synthesis of defect-engineered graphitic carbon nitride nanotubes for efficient conversion of solar energy, *Appl. Catal. B-Environ.* 225 (2018) 154–161.
- C.Y. Zhou, P. Xu, C. Lai, C. Zhang, G.M. Zeng, D.L. Huang, M. Cheng, L. Hu, W.P. Xiong, X.F. Wen, L. Qin, J.L. Yuan, W.J. Wang, Rational design of graphitic carbon nitride copolymers by molecular doping for visible-light-driven degradation of aqueous sulfamethazine and hydrogen evolution, *Chem. Eng. J.* 359 (2019) 186–196.
- J.G. Hou, H.J. Cheng, O. Takeda, H.M. Zhu, Unique 3D heterojunction photoanode design to harness charge transfer for efficient and stable photoelectrochemical water splitting, *Energy Environ. Sci.* 8 (2015) 1348–1357.
- F. Wang, J.C. Jiang, K. Wang, Q.L. Zhai, F. Long, P. Liu, J.F. Feng, H.H. Xia, J. Ye, J. Li, J.M. Xu, Hydrotreatment of lipid model for diesel-like alkane using nitrogen-doped mesoporous carbon-supported molybdenum carbide, *Appl. Catal. B-Environ.* 242 (2019) 150–160.
- L. Tian, X.F. Yang, Q.Q. Liu, F.Q. Qu, H. Tang, Anchoring metal-organic framework nanoparticles on graphitic carbon nitrides for solar-driven photocatalytic hydrogen evolution, *Appl. Surf. Sci.* 455 (2018) 403–409.
- L. Li, W. Fang, P. Zhang, J. Bi, Y. He, J. Wang, W. Su, Sulfur-doped covalent triazine-based frameworks for enhanced photocatalytic hydrogen evolution from water under visible light, *J. Mater. Chem. A Mater. Energy Sustain.* 4 (2016) 12402–12406.
- J.X. Xu, S.W. Cao, T. Brenner, X.F. Yang, J.G. Yu, M. Antonietti, M. Shalom, Supramolecular chemistry in molten sulfur: preorganization effects leading to marked enhancement of carbon nitride photoelectrochemistry, *Adv. Funct. Mater.* 25 (2015) 6265–6271.
- S. Kuecken, A. Acharjya, L. Zhi, M. Schwarze, R. Schomäcker, A. Thomas, Fast tuning of covalent triazine frameworks for photocatalytic hydrogen evolution, *Chem. Commun.* 53 (2017) 5854–5857.
- Z.P. Chen, S. Pronkin, T.P. Fellingner, K. Kailasam, G. Vile, D. Albani, F. Krumeich, R. Leary, J. Barnard, J.M. Thomas, J. Perez-Ramirez, M. Antonietti, D. Dontsova, Merging Single-Atom-Dispersed Silver and Carbon Nitride to a Joint Electronic System via Copolymerization with Silver Tricyanomethanide, *ACS Nano* 10 (2016) 3166–3175.
- Y. Ishida, L. Chabanne, M. Antonietti, M. Shalom, Morphology control and photocatalysis enhancement by the one-pot synthesis of carbon nitride from preorganized hydrogen-bonded supramolecular precursors, *Langmuir* 30 (2014) 447–451.
- G.G. Zhang, L.H. Lin, G.S. Li, Y.F. Zhang, A. Savateev, S. Zafeirotas, X.C. Wang, M. Antonietti, Ionothermal synthesis of triazine-heptazine-based copolymers with apparent quantum yields of 60% at 420 nm for solar hydrogen production from "Sea Water", *Angew. Chem. Int. Ed.* 57 (2018) 9372–9376.
- K. Schwinghammer, S. Hug, M.B. Mesch, J. Senker, B.V. Lotsch, Phenyl-triazine oligomers for light-driven hydrogen evolution, *Energy Environ. Sci.* 8 (2015) 3345–3353.
- Y. Zheng, L.H. Lin, B. Wang, X.C. Wang, Graphitic carbon nitride polymers toward sustainable photoredox catalysis, *Angew. Chem. Int. Ed.* 54 (2015) 12868–12884.
- Z.F. Chen, S.C. Lu, Q.L. Wu, F. He, N.Q. Zhao, C.N.A. He, C.S. Shi, Salt-assisted synthesis of 3D open porous g-C<sub>3</sub>N<sub>4</sub> decorated with cyano groups for photocatalytic hydrogen evolution, *Nanoscale* 10 (2018) 3008–3013.
- W.N. Xing, W.G. Tu, Z.H. Han, Y.D. Hu, Q.Q. Meng, G. Chen, Template-induced high-crystalline g-C<sub>3</sub>N<sub>4</sub> nanosheets for enhanced photocatalytic H<sub>2</sub> evolution, *ACS Energy Lett.* 3 (2018) 514–519.
- Z.P. Chen, A. Savateev, S. Pronkin, V. Papaefthimiou, C. Wolff, M.G. Willinger, E. Willinger, D. Neher, M. Antonietti, D. Dontsova, "The easier the better" preparation of efficient photocatalysts-metastable poly(heptazine imide) salts, *Adv. Mater.* 29 (2017) 1700555.
- J.S. Xu, H. Wang, C. Zhang, X.F. Yang, S.W. Cao, J.G. Yu, M. Shalom, From millimeter to subnanometer: vapor-solid deposition of carbon nitride hierarchical nanostructures directed by supramolecular assembly, *Angew. Chem. Int. Ed.* 56 (2017) 8426–8430.
- X.F. Yang, H. Tang, J.S. Xu, M. Antonietti, M. Shalom, Silver Phosphate/Graphitic carbon nitride as an efficient photocatalytic tandem system for oxygen evolution, *ChemSusChem* 8 (2015) 1350–1358.
- Y.S. Jun, E.Z. Lee, X.C. Wang, W.H. Hong, G.D. Stucky, A. Thomas, From melamine-cyanuric acid supramolecular aggregates to carbon nitride hollow spheres, *Adv. Funct. Mater.* 23 (2013) 3661–3667.
- M. Shalom, S. Inal, C. Fettkenhauer, D. Neher, M. Antonietti, Improving carbon nitride photocatalysis by supramolecular preorganization of monomers, *J. Am. Chem. Soc.* 135 (2013) 7118–7121.
- W.D. Li, Y. Liu, M. Wu, X.L. Feng, S.A.T. Redfern, Y. Shang, X. Yong, T. Feng, K.F. Wu, Z.Y. Liu, B.J. Li, Z.M. Chen, J.S. Tse, S.Y. Lu, B. Yang, Carbon-quantum-Dots-Loaded ruthenium nanoparticles as an efficient electrocatalyst for hydrogen production in alkaline media, *Adv. Mater.* 30 (2018) 1800676.
- Y. Yu, W. Yan, W. Gao, P. Li, X. Wang, S. Wu, W. Song, K. Ding, Aromatic ring substituted g-C<sub>3</sub>N<sub>4</sub> for enhanced photocatalytic hydrogen evolution, *J. Mater. Chem. A* 5 (2017) 17199–17203.
- X. Wang, K. Maeda, A. Thomas, K. Takanabe, G. Xin, J.M. Carlsson, K. Domen, M. Antonietti, A metal-free polymeric photocatalyst for hydrogen production from water under visible light, *Nat. Mater.* 8 (2008) 76–80.
- Q. Han, B. Wang, J. Gao, Z. Cheng, Y. Zhao, Z. Zhang, L. Qu, Atomically thin mesoporous nanomesh of graphitic C<sub>3</sub>N<sub>4</sub> for high-efficiency photocatalytic hydrogen evolution, *ACS Nano* 10 (2016) 2745–2751.
- Q. Wang, S. Guan, B. Li, 2D graphitic-C<sub>3</sub>N<sub>4</sub> hybridized with 1D flux-grown Na-modified K<sub>2</sub>Ti<sub>6</sub>O<sub>13</sub> nanobelts for enhanced simulated sunlight and visible-light photocatalytic performance, *Catal. Sci. Technol.* 7 (2017) 4064–4078.



- [51] S. Chu, C.C. Wang, J.Y. Feng, Y. Wang, Z.G. Zou, Melem: a metal-free unit for photocatalytic hydrogen evolution, *Int. J. Hydrogen Energy* 39 (2014) 13519–13526.
- [52] P. Yang, R. Wang, M. Zhou, X. Wang, Photochemical construction of carbonitride structures for red-light redox catalysis, *Angew. Chem. Int. Ed.* 57 (2018) 8674–8677.
- [53] J.E. Nutting, M. Rafiee, S.S. Stahl, Tetramethylpiperidine N-Oxyl (TEMPO), phthalimide N-Oxyl (PINO), and related N-Oxyl species: electrochemical properties and their use in electrocatalytic reactions, *Chem. Rev.* 118 (2018) 4834–4885.
- [54] M.Z. Rahman, C.B. Mullins, Understanding charge transport in carbon nitride for enhanced photocatalytic solar fuel production, *Acc. Chem. Res.* 52 (2019) 248–257.
- [55] H. Zhang, Y. Chen, R. Lu, R. Li, A. Yu, Charge carrier kinetics of carbon nitride colloid: a femtosecond transient absorption spectroscopy study, *Phys. Chem. Chem. Phys.* 18 (2016) 14904–14910.
- [56] S.R. Pendlebury, X. Wang, F. Le Formal, M. Cornuz, A. Kafizas, S.D. Tilley, M. Gratzel, J.R. Durrant, Ultrafast charge carrier recombination and trapping in hematite photoanodes under applied bias, *J. Am. Chem. Soc.* 136 (2014) 9854–9857.
- [57] Z. Chen, Q. Zhang, Y. Luo, Experimental identification of ultrafast reverse hole transfer at the interface of the photoexcited Methanol/Graphitic carbon nitride system, *Angew. Chem. Int. Ed.* 57 (2018) 5320–5324.
- [58] W.A. Tisdale, K.J. Williams, B.A. Timp, D.J. Norris, E.S. Aydil, X.Y. Zhu, Hot-electron transfer from semiconductor nanocrystals, *Science* 328 (2010) 1543–1547.
- [59] H.Q. Xu, J.H. Hu, D.K. Wang, Z.H. Li, Q. Zhang, Y. Luo, S.H. Yu, H.L. Jiang, Visible-light photoreduction of CO<sub>2</sub> in a metal-organic framework: boosting electron-hole separation via Electron trap states, *J. Am. Chem. Soc.* 137 (2015) 13440–13443.
- [60] D.A. Wheeler, J.Z. Zhang, Exciton dynamics in semiconductor nanocrystals, *Adv. Mater.* 25 (2013) 2878–2896.
- [61] W.J. Ong, L.K. Putri, Y.C. Tan, L.L. Tan, N. Li, Y.H. Ng, X.M. Wen, S.P. Chai, Unravelling charge carrier dynamics in protonated g-C<sub>3</sub>N<sub>4</sub> interfaced with carbon nanodots as co-catalysts toward enhanced photocatalytic CO<sub>2</sub> reduction: a combined experimental and first-principles DFT study, *Nano Res.* 10 (2017) 1673–1696.
- [62] Z. Mo, H. Xu, Z. Chen, X. She, Y. Song, J. Wu, P. Yan, L. Xu, Y. Lei, S. Yuan, H. Li, Self-assembled synthesis of defect-engineered graphitic carbon nitride nanotubes for efficient conversion of solar energy, *Appl. Catal. B-Environ.* 225 (2018) 154–161.